RSC Advances

PAPER

View Article Online
View Journal | View Issue

Cite this: *RSC Adv.*, 2025, **15**, 7248

Preparation of hydrophilic and antifouling coatings *via* tannic acid and zwitterionic polymers†

Aosheng Zhong,[a] Ruixiang Tao,[b] Ran Zong,[a] Shuangyi Liu[a] and Baoqing Shentu*[a]

Received 27th January 2025
Accepted 27th February 2025

DOI: 10.1039/d5ra00643k

rsc.li/rsc-advances

The attachment and colonization of proteins and bacteria on the surface of implantable medical materials can lead to biofilm formation, which in turn promotes inflammation and increases the treatment burden. This study developed a hydrophilic coating with excellent adhesion and antifouling lubrication properties, by exploiting the adhesive capability of tannic acid (TA) and the antifouling zwitterionic polymer. TA–Fe^{3+} complex *via* coordination interactions formed a thin layer on the surface of polyethylene terephthalate (PET) and then poly(ethylenimine)-*g*-sulfobetaine methacrylate (PEI-*g*-SBMA) underwent a Schiff-base reaction with the TA layer, allowing the zwitterionic copolymer to be anchored onto the PET surface. Elemental and morphological surface analyses successfully confirmed the deposition of TA–Fe^{3+} complex and PEI-*g*-SBMA onto the surfaces. Water contact angle and friction coefficient tests indicated an improvement in the hydrophilic and lubricating properties of the surface after modification. Importantly, the modified surfaces exhibited a significant reduction in the adsorption of bovine serum albumin (BSA), demonstrating the excellent antifouling ability. Hemolysis tests were also conducted to assess the hemocompatibility of the coatings. The results indicated that lubricative and antifouling coatings can be easily prepared on medical material surfaces using the approach, which showed significant potential for applications in biomedical fields.

1. Introduction

In the field of interventional medicine, devices such as heart valves, artificial blood vessels, and catheters are widely used.[1] These devices are commonly fabricated from polymeric materials, such as polyethylene terephthalate (PET), polyurethane (PU), and polyvinyl chloride (PVC), which are characterized by high mechanical strength, elasticity, and biocompatibility. Consequently, they are widely employed in implantation and interventional medical applications.[2,3] The increasing use of medical devices has resulted in a growing prevalence of device-associated infections, presenting significant challenges for both healthcare professionals and patients.[4] The hydrophobic properties of catheter materials promote microbial adhesion and colonization, which contribute to biofilm formation—a key factor in the onset of infections. Consequently, this reduces the effective lifespan of the catheters and complicates the diagnosis and treatment of various medical conditions.[5] Moreover, since catheters are in constant and direct contact with soft tissues, their surfaces must exhibit superior lubricating properties. This is crucial not only for reducing patient discomfort during insertion and prolonged use, but also for protecting mucosal and other soft tissues from injury, thereby preventing infections and related complications.[6,7] Therefore, surface modification is essential to enhance the catheter's hydrophilicity, ensuring both resistance to biofouling and improved lubrication.[8,9]

Zwitterionic polymers, characterized by the presence of both positive and negative charges in equal amounts, demonstrate excellent hydrophilicity and biocompatibility.[10] Unlike conventional hydrophilic polymers such as polyethylene glycol, zwitterionic materials induce ionic solvation through electrostatic interactions, which facilitate the formation of a hydration layer on the material surface. This hydration layer, which is more robust and compact than hydrogen-bond interaction, effectively prevents protein adhesion and exhibits superior antifouling properties.[11,12] Zwitterionic polymers are emerging as promising candidates for next-generation antifouling materials[13] and have been extensively applied in areas such as cardiovascular devices, blood purification systems, extracorporeal membrane oxygenation (ECMO) and orthopedic lubricants.[14–17] He *et al.*[18] constructed a poly(sulfobetaine methacrylate) (PSBMA) modified coating on the poly-4-methyl-1-pentene (PMP) surface, which is used in the core component of ECMO membrane oxygenators. Following modification, protein adsorption on the PMP membrane was reduced by 70.58%, and its blood compatibility was significantly enhanced. *In vitro* blood circulation tests further demonstrated that the modified coating exhibited excellent oxygenation performance and biological

[a]*State Key Laboratory of Chemical Engineering, College of Chemical and Biological Engineering, Zhejiang University, Hangzhou, 310058, China. E-mail: shentu@zju.edu.cn*

[b]*Zhejiang CHINT Cable Co., Ltd., Jiaxing 314006, China*

† Electronic supplementary information (ESI) available. See DOI: https://doi.org/10.1039/d5ra00643k

safety. Li *et al.*[19] developed a sulfo-betaine zwitterionic hydrogel microgel coating for artificial blood vessels, which adheres to the surface of blood-contacting medical catheters through hydrogen bonding. After modification, the surface water contact angle was reduced to 6.9°, and the friction coefficient decreased to 0.0017. The coating effectively resisted the adhesion of blood components and inhibited thrombotic and inflammatory responses, providing a novel, safe, and versatile strategy for preventing thrombosis and inflammation in a wide range of blood-contacting medical devices.

Surface grafting techniques are widely employed to prepare zwitterionic polymer coatings on material surfaces, providing high grafting density and stability.[20,21] For example,[22] Yao *et al.*[23] embedded the hydrophobic photoinitiator benzophenone into the PVC substrate to graft polycarboxybetaine/poly-sulfbetaine hydrogel coatings. *In vitro* circulation experiments demonstrated a significant reduction in foreign body reactions and prevention of thrombus formation. Wang *et al.*[24] used a two-step method involving dip-coating and *in situ* UV polymerization to prepare flexible poly (sulfobetaine methacrylate) (PSBMA) coatings with self-healing, antifouling, and lubricating properties. These coatings effectively resisted non-specific protein adsorption and inhibited cell and platelet adhesion, showing strong potential for use in various implantable medical devices. However, this method has limitations regarding the types of materials it can be applied to, as it is unsuitable for silicone-based materials, such as silicone rubber. Moreover, UV curing equipment must be adapted for materials with different shapes and specifications.

In recent years, catechol-based biofouling-resistant surfaces inspired by mussels have attracted significant attention.[25–28] Tannic acid (TA), when complexed with Fe^{3+}, rapidly forms ultrathin coatings on a variety of material surfaces. Compared to polydopamine (PDA)-based coatings, TA-based coatings offer faster adhesion, lower cost, and enhanced functionality. Since its first report in 2013,[29] surface modification using TA has garnered considerable interest due to the high content of catechol groups in tannic acid, which provides strong adhesion to a wide range of materials.[30–32] For instance, Kim *et al.*[33] quickly assembled a multifunctional coating of tannic acid and iron ions on commercial polyethersulfone membranes, creating a filter with antifouling properties against proteins, oils, and microorganisms, as well as antibacterial and heavy metal ion removal capabilities. Xie *et al.*[34] co-deposited silver nanoparticles and zwitterionic polymers onto TA-modified polyethersulfone (PES) surfaces. The modified surfaces exhibited an ultra-hydrophilic contact angle of <10°, along with antifouling and antimicrobial properties.

Based on the excellent adhesion properties of tannic acid (TA), the TA–Fe^{3+} complex was initially deposited on the material surface through a rapid coordination reaction between TA and Fe^{3+}, forming a TA–Fe^{3+} film. This film imparts enhanced hydrophilicity to the material surface. Polyethyleneimine (PEI) was then grafted with sulfobetaine methacrylate (SBMA), yielding a reactive zwitterionic graft copolymer, PEI-*g*-PSBMA. The PEI-*g*-PSBMA was subsequently introduced and anchored onto the material surface *via* Schiff base reactions with TA. As a functional polymer, PEI-*g*-PSBMA provides the material with resistance to biofouling. The chemical composition of the material surface was characterized using scanning electron microscopy (SEM) coupled with energy dispersive spectroscopy (EDS) and X-ray photoelectron spectroscopy (XPS). The hydrophilicity of the material was evaluated through water contact angle measurements, while the biofouling resistance and friction coefficient of the coating were also examined.

2. Experimental section

2.1. Materials

Polyethyleneimine (PEI, branched, M_w = 10 000), sulfobetaine methacrylate (SBMA, 97%), tannic acid (TA, 95%), *tert*-butyl hydroperoxide (TBHP, 70% aqueous solution), ferric chloride hexahydrate ($FeCl_3 \cdot 6H_2O$, 99%), and phosphate-buffered saline (PBS, pH = 8.5) were purchased from Shanghai Aladdin Biochemical Technology Co., Ltd. Polyethylene terephthalate (PET) sheets were purchased from Guangdong Wangbang Materials Co., Ltd. The BCA Protein Assay Kit (500T) was purchased from Shanghai Beyotime Biotechnology Co., Ltd. Fresh bovine blood was purchased from Beijing Solarbio Technology Co., Ltd. Deionized water used in the experiments had a resistivity of 18.5 MΩ cm. All materials were used directly unless otherwise specified.

2.2. Deposition of TA–Fe^{3+} complex on PET surfaces

The TA–Fe^{3+} complex was deposited onto the PET surface using two different methods. For the one-pot deposition process, the TA aqueous solution (4 mg mL^{-1}) was mixed with $FeCl_3 \cdot 6H_2O$ aqueous solution (1 mg mL^{-1}). The PET substrate, pre-soaked in ethanol, was immersed in the complex solution for 5 minutes, then removed, rinsed with deionized water, and dried under a nitrogen atmosphere. But for the two-pot deposition process, the PET substrate was first immersed in the TA aqueous solution (4 mg mL^{-1}) for 5 minutes after being pre-soaked in ethanol. After rinsing with deionized water to remove unstable adsorbed TA molecules, the substrate was transferred to the $FeCl_3 \cdot 6H_2O$ solution (1 mg mL^{-1}) for 5 minutes. The subsequent drying treatment was the same as described previously. This process was repeated 1, 3, and 5 times to prepare three TA–Fe^{3+} complexes. The mass of the PET samples before and after deposition of the TA–Fe^{3+} complex was measured to determine the relative mass increase.

2.3. Synthesis of PEI-*g*-SBMA and the preparation of antifouling surfaces

As shown in Scheme 1, PEI-*g*-SBMA was synthesized by using the Michael addition reaction as reported in previous studies.[35,36] By varying the feed molar amount of SBMA, a set of graft copolymers were synthesized, named PEI-*g*-SBMA$_x$, where x represents the mass percentage of SBMA in the copolymer. PEI-*g*-SBMA was attached onto the TA–Fe^{3+}/PET surface *via* the Schiff-base reaction. PEI-*g*-SBMA$_x$ was dissolved in PBS buffer to achieve a solution with a concentration of 20 mg mL^{-1} and a pH of 8.5. The TA–Fe^{3+}/PET substrate was immersed in this

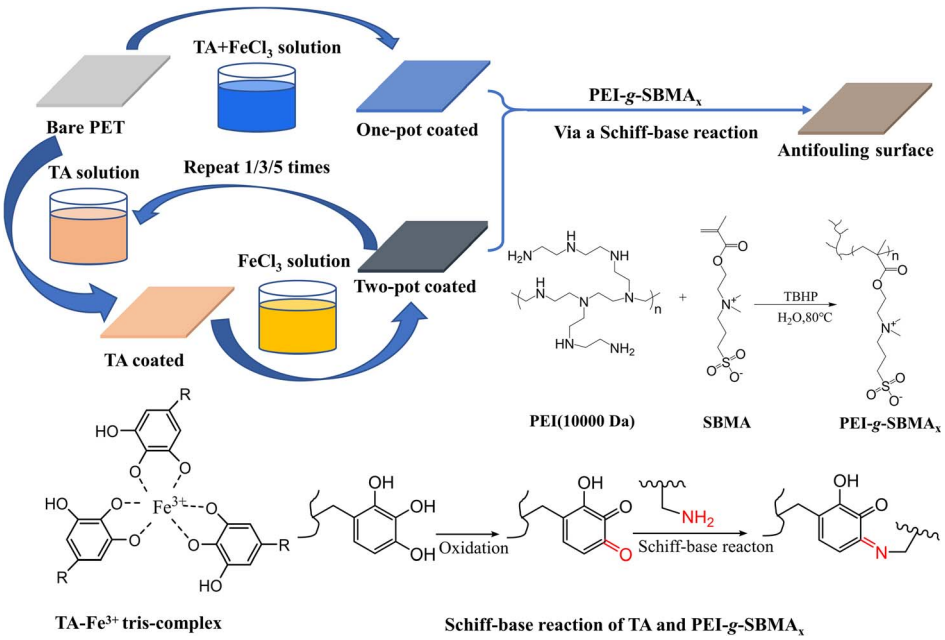

Scheme 1 Preparation process of antifouling PEI-*g*-SBMA$_x$/TA–Fe^{3+}/PET composite.

solution for 12 hours, then removed, gently rinsed with deionized water, and dried under a nitrogen atmosphere. The resulting modified samples were named as PEI-*g*-SBMA$_x$/TA–Fe^{3+}/PET.

2.4. Characterization of PEI-*g*-SBMA$_x$

The ^{1}H NMR spectra were recorded at 500 MHz with a Bruker NMR Systems (AVANCE NEO, Germany) using D_2O as the solvent. The Fourier transform infrared spectroscopy spectra of PEI-*g*-SBMA$_x$ were obtained by ATR method using a FTIR spectrometer (Nicolet iS50, America).

2.5. Characterization and stability of TA–Fe^{3+} complex on PET surfaces

The elemental composition and content of the surfaces were analyzed using energy dispersive spectroscopy (EDS) attached to the SEM (SU-3500, Japan) and XPS (Escalab 250Xi, America). The cross-sectional and surface morphologies were obtained by SEM (SU-8010, Japan). The film thickness distribution was obtained by measuring the film thickness of at least 50 different images of each layer. The effect of deposition times on the surface morphology of TA–Fe^{3+} complex was studied using atomic force microscopy (AFM) (Multimode, America). The surface roughness of different deposition times was also recorded.

The surface hydrophilicity was evaluated using a video optical contact angle goniometer (OCA 20, Germany). For each measurement, a 5 μL water droplet was applied, and the contact angle was measured at three different locations on the surface. The average contact angle was calculated from these measurements.

In order to evaluate the adhesion stability of the TA–Fe^{3+} complex on PET surface, the TA–Fe^{3+}/PET substrates were cut into 0.5 cm × 0.5 cm pieces and immersed in 10 mL of deionized water with ultrasonic treatment for one hour. Subsequently, the absorbance of the solution was measured using a UV-vis spectrophotometer (Shimadzu UV-2600, Japan). A 0.4 mg per mL TA aqueous solution was used as the control group.

2.6. Characterization of PEI-*g*-SBMA$_x$/TA–Fe^{3+}/PET surfaces

The elemental composition and content of the surfaces were analyzed using energy dispersive spectroscopy (EDS) attached to the SEM (SU-3500, Japan) and XPS (Escalab 250Xi, America).

The friction coefficient of the surface was measured using a friction and wear testing machine (UTM-3, USA).

Evaluation of anti-biofouling performance was *via* bovine serum albumin (BSA) adsorption experiment. The BSA adsorption experiment was conducted according to the instructions of the BCA Protein Concentration Assay Kit (P0012 500T, Beyotime). Specifically, the PEI-*g*-SBMA$_x$/TA–Fe^{3+}/PET samples were cut into 1 cm × 1 cm pieces and incubated with 5 mL of 1 mg per mL BSA phosphate-buffered solution at 37 °C for 2 hours. After incubation, the samples were sequentially washed twice with deionized water and PBS buffer to remove the free BSA on the surfaces. The samples were then incubated with 5 mL of 2 wt% sodium dodecyl sulfate (SDS) aqueous solution at 37 °C for one hour to remove the adsorbing BSA on the surfaces. The absorbance of solution at 562 nm was measured using a microplate reader (ReadMax 1900, China).

2.7. Hemolysis ratio test

Hemolysis evaluation was performed to assess the hemocompatibility of PEI-*g*-SBMA$_x$/TA–Fe^{3+}/PET. Sterile fresh bovine blood (5 mL) was added to a centrifuge tube containing 20 mL of PBS buffer. The mixture was centrifuged at 2500 rpm for 10

minutes, and the supernatant was removed. This washing step was repeated 4–5 times until the supernatant became clear. The washed red blood cells were then prepared into a 4% red blood cell suspension for use. The samples were cut into 0.5 cm × 0.5 cm pieces and incubated with 0.5 mL of the 4% red blood cell suspension and 4 mL of PBS buffer at 37 °C with shaking at 100 rpm for 2 hours. After centrifuging at 3000 rpm, the supernatant was collected, and the absorbance at 545 nm was measured. The positive control group consisted of 0.5 mL of the 4% red blood cell suspension and 4 mL of deionized water, while the negative control group consisted of 0.5 mL of the 4% red blood cell suspension and 4 mL of PBS buffer. The hemolysis rate was calculated using the following formula: hemolysis ratio (%) = $((OD_{test} - OD_{negative}) - (OD_{positive} - OD_{negative})) \times 100\%$.

3. Results and discussion

3.1. Characterization of TA–Fe^{3+}/PET surfaces

The TA/Fe^{3+} complexes were deposited onto the PET surfaces using both the one-pot method for single-step self-assembly and the two-pot method for multi-step self-assembly. XPS results showed that TA–Fe^{3+} complexes were successfully deposited on PET surfaces by both methods. As shown in Fig. 1a, compared to the original PET surface, Fe characteristic peak was observed in the 680 eV to 760 eV range on the surfaces prepared by both the one-step and multi-step self-assembly methods. The chemical composition and weight gain percentages of the TA–Fe^{3+} deposited surfaces are shown in Table 1. In the one-pot method, the atomic percentage of Fe in the TA–Fe^{3+} complex was 0.56%, while for the one-step assembly in the two-pot method, the Fe atomic percentage on the surface of the TA–Fe^{3+} complex was 0.94%. Additionally, the weight increase of PET after deposited with the TA–Fe^{3+} complex was compared. After the one-pot method, the PET mass increased by 0.89%, while after the one-step assembly using the two-pot method, the mass increased by 1.24%. This result can primarily be attributed to the different process in the two methods. In the one-pot method process, the complexation of tannic acid with iron ions occurred at the moment TA and Fe^{3+} solutions were mixed.[37] Due to the strong chelating ability between tannic acid and iron ions, this results in the aggregation of a large number of tannic acid molecules into clusters. This aggregation hinders the diffusion of iron ions onto the PET surface. In contrast, in the two-pot method, the PET substrate was first immersed in the tannic acid solution, allowing tannic acid to adsorb onto the

Table 1 Surface elemental compositions of PET and TA–Fe^{3+}/PET using EDS, and weight gain after deposition

	Atom ratio (%)			
Entry	C	O	Fe	Weight gain (wt%)
PET	67.74	32.26	—	—
One-pot	64.88	34.56	0.56	0.89
Two-pot 1 layer	64.00	35.06	0.94	1.24
Two-pot 3 layers	61.44	36.88	1.68	3.58
Two-pot 5 layers	60.19	37.22	2.59	6.44

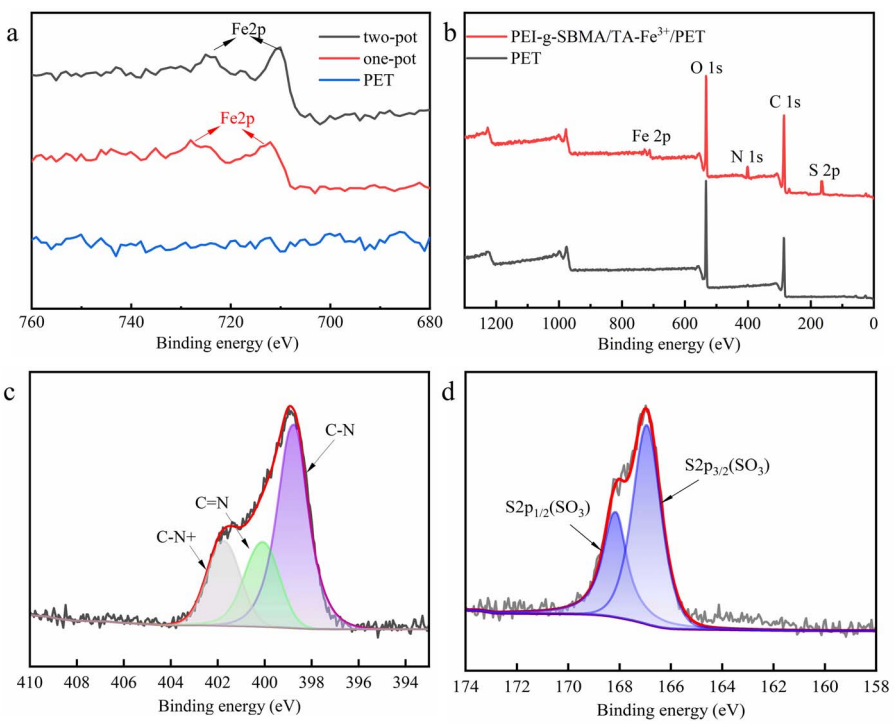

Fig. 1 Fe 2p spectra for the TA–Fe^{3+}/PET (a); XPS wide spectra of the PEI-*g*-SBMA/TA-Fe^{3+}/PET (b); N 1s spectra for the PEI-*g*-SBMA/TA–Fe^{3+}/PET (c); S 2p spectra for the PEI-*g*-SBMA/TA–Fe^{3+}/PET (d), respectively.

PET surface through hydrogen bonding, π–π stacking, and hydrophobic interactions.[38] Moreover, the independent tannic acid molecules had smaller steric hindrance compared to the large TA–Fe^{3+} complex molecules, which facilitates adsorption. This leaded to a higher adsorption amount of tannic acid, as finally reflected in increase of both the Fe^{3+} percentage of on the surface the surface and the weight after depositing.

Furthermore, as the number of self-assembly steps in the two-pot method increased, the amount of tannic acid adsorbed also rose. After five self-assembly steps, the atomic percentage of Fe^{3+} on the PET surface increased to 2.59%, and the weight gain increased by 6.44% (Table 1). As shown in Fig. 2a, the SEM images of TA–Fe^{3+} complexes deposited by two-pot method were illustrated. With the increase of deposition times, the nano-structured protrusions on the films increased. Additionally, a few particles which should be originated from the TA–Fe^{3+} aggregates were observed. This is due to the fact that TA has a substrate independent coating behaviour during the first assembly of TA. TA molecules are easily coated on the PET surfaces, and then Fe^{3+} coordinates with catecholic groups of TA to complete the first layer of deposition.

In the subsequent deposition, both the free TA molecules and the TA aggregates resulted from oxidation self-polymerization in solution can coordinate with the Fe^{3+} already deposited in the first layer, which leads the formation of protrusions and non-homogeneity on the film surface. The AFM topography images (Fig. 2b) showed that the roughness of TA–Fe^{3+} complex films increased with the increase of deposition times, which further confirmed that the size of the nano-structured protrusions on the film increased to submicron

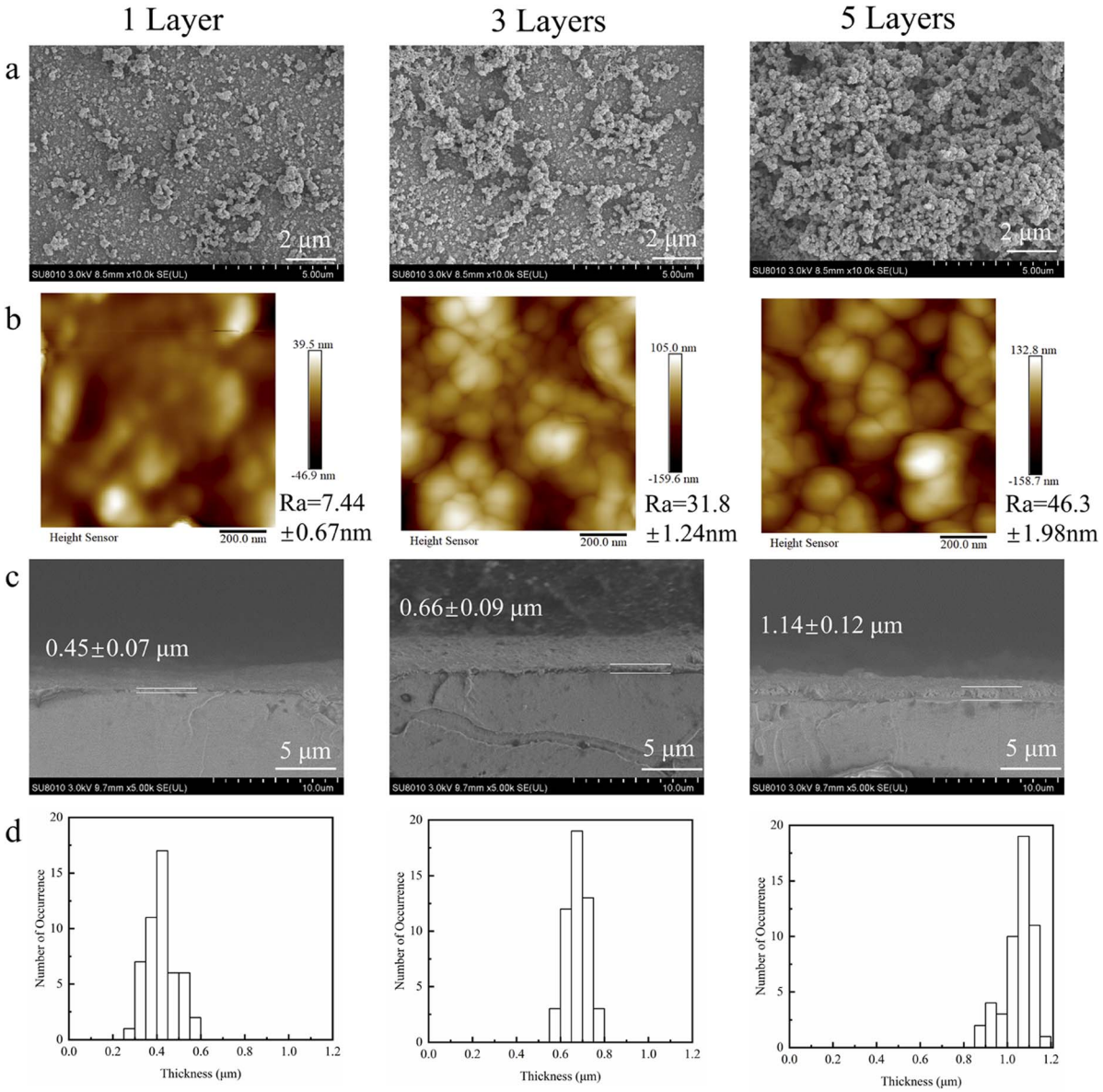

Fig. 2 Surface SEM images (a); AFM surface topography images (b); cross-sectional SEM images (c); TA–Fe^{3+} complex film thickness distribution (d) of TA–Fe^{3+}/PET by two-pot process: 1 layer; 3 layers; 5 layers, respectively.

and the surface become rougher. The cross-sectional SEM images (Fig. 2c) showed that the thickness of the TA–Fe^{3+} complex films increased with the number of self-assembly steps. The TA–Fe^{3+} film thickness after once, three, and five times deposition was 0.45 ± 0.07 μm, 0.66 ± 0.09 μm and 1.14 ± 0.12 μm, respectively. In order to investigate the statistical distribution of the film thickness, the film thickness of 50 cross sections under the same deposition times was collected, and the film thickness distribution was shown in Fig. 2d.[39–41] It could be clearly seen that the film thickness tends to become thicker with the increase of deposition times. The thickness of TA–Fe^{3+} complex film can be controlled by changing the number of self-assembly steps.

The deposition of TA–Fe^{3+} complex onto the PET surfaces enhanced hydrophilic property. As shown in Fig. 3a, the initial water contact angle of the hydrophobic PET surface was 92°. Tannic acid molecules, which are rich in phenolic hydroxyl groups, can enhance the hydrophilicity as the amount of tannic acid adsorption increased. After deposition by one-pot method, the water contact angle on the surface decreased to 76°. In the two-pot method, with an increasing number of self-assembly cycles, the water contact angle decreased further, reaching 16° after five cycles. These results indicated a significant improvement in the hydrophilic property following the deposition of TA–Fe^{3+} complex. Additionally, it is crucial that the TA–Fe^{3+} deposition adheres stably onto the PET surface. In order to evaluate the adhesion stability of the TA–Fe^{3+}/PET, the samples were immersed in deionized water and subjected to ultrasonic treatment, and the absorbance of the solution was measured to determine if TA molecules were released from the PET surface. As shown in Fig. 3b, despite the high-energy impact of the ultrasound, the TA–Fe^{3+} complex deposited by both two methods exhibited excellent adhesion to the PET substrates. This result suggests that, with stable adhesion, other functional molecules can be further introduced onto the TA–Fe^{3+}/PET surface.

3.2. Characterization of PEI-*g*-SBMA/TA–Fe^{3+}/PET surfaces

By varying the molar ratio of the polymer PEI to the monomer SBMA, as illustrated in Scheme 1, three grafted copolymers, PEI-*g*-SBMA with different SBMA contents were synthesized. Their ^{1}H NMR spectra were shown in Fig. 4a, compared with the spectrum of PEI, some new peaks appeared in the spectra of PEI-*g*-SBMA, which were marked as a, b, c, d, e, f, g, and h. The proton peaks at d, e, and f corresponded to the carbon atoms attached to the nitrogen atom in SBMA, the proton peak at h represented the signal of the α-carbon atom bonded to the sulfonic group in SBMA, and the proton peak at g corresponded to the signal of the β-carbon atom linked to the sulfonic group. Three grafted copolymers, PEI-*g*-$SBMA_{12\%}$, PEI-*g*-$SBMA_{22\%}$, and PEI-*g*-$SBMA_{40\%}$, with grafting ratios (weight percentage of SBMA) of 12%, 22%, and 40%, respectively, were synthesized. The FTIR spectra (Fig. 4b) were also used to ascertain the structure of copolymers. Compared with the original PEI infrared spectrum, new peaks appeared at 1725 cm^{-1} and 1175 cm^{-1}, corresponding to the characteristic absorption peaks of C=O and C–O–C stretching vibrations in –COOR,

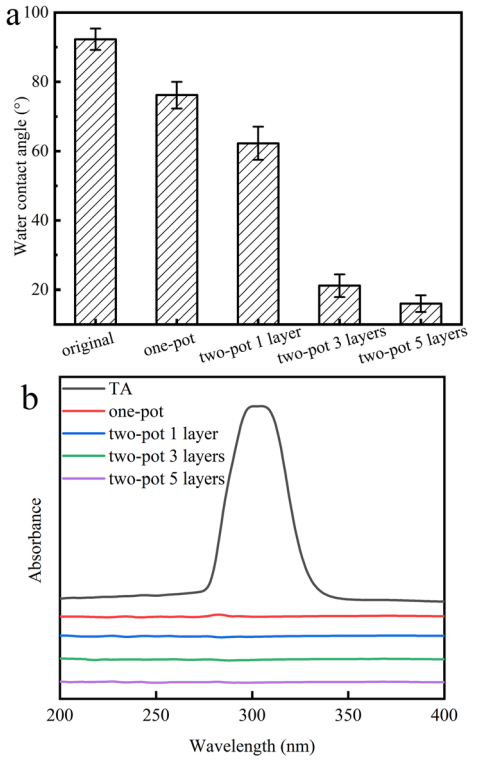

Fig. 3 Water contact angle of TA–Fe^{3+}/PET (a); absorbance of solution after ultrasonic treatment of TA–Fe^{3+}/PET, the control group: a 0.4 mg mL^{-1} TA aqueous solution (b).

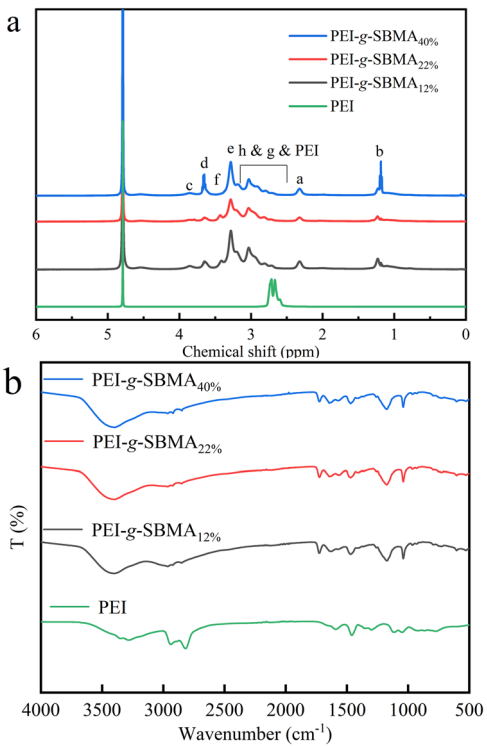

Fig. 4 ^{1}H NMR spectra of PEI, PEI-*g*-$SBMA_x$ (a); FTIR spectra of PEI, PEI-*g*-$SBMA_x$ (b).

Table 2 Surface elemental compositions of PEI-*g*-SBMA$_x$/TA–Fe^{3+}/PET using EDS

	Atom ratio (%)				
Entry	C	O	Fe	N	S
PET	67.74	32.26	—	—	—
PEI-*g*-SBMA$_{12\%}$/TA–Fe^{3+}/PET	60.38	33.70	1.26	4.54	0.12
PEI-*g*-SBMA$_{22\%}$/TA–Fe^{3+}/PET	59.31	34.62	1.19	4.72	0.16
PEI-*g*-SBMA$_{40\%}$/TA–Fe^{3+}/PET	59.17	34.52	1.21	4.88	0.22

respectively. The peak at 1045 cm^{-1} corresponded to the characteristic stretching vibration of –SO_3. The results confirmed the successful synthesis of three copolymers with different grafting ratio.

Similarly, the chemical elemental composition of the PEI-*g*-SBMA/TA–Fe^{3+}/PET surfaces was characterized by EDS (Table 2) (ESI†). The original PET surface contained only carbon (C) and oxygen (O). TA molecules, which contain numerous phenolic hydroxyl groups, are prone to oxidation into quinone structures, as shown in Scheme 1. The amino (–NH_2) groups of the PEI-*g*-SBMA copolymer react with the carbonyl groups of the quinone structure in TA through a Schiff-base reaction, forming chemical bonds and anchoring the polymer onto the TA–Fe^{3+}/PET surface. This process resulted in the attachment of zwitterionic polymer to the PET surface. So two new elements nitrogen (N) and sulfur (S) were introduced, and content of S increased with the higher grafting ratio of SBMA as expected. The wide-scan XPS spectrum (Fig. 1b) revealed that the original PET surface exhibited two elements for C 1s (284.6 eV) and O 1s (531.6 eV). After the PEI-*g*-SBMA was grafted onto the TA–Fe^{3+}/PET surface, significant new element signals were observed, corresponding to the PEI-*g*-SBMA: N 1s (398.7 eV) and S 2p (167.1 eV) peaks. The high-resolution element scan spectra were as shown in Fig. 1c and d. The N 1s spectrum was fitted with three peaks, with the new C=N bond peak (399.2 eV) indicating that the PEI-*g*-SBMA was covalently bonded to the TA–Fe^{3+} complex *via* Schiff-base reaction. The C–N$^+$ bond peak (401.7 eV) corresponded to the quaternary ammonium salt structure in SBMA. Meanwhile, the S 2p spectrum was fitted with two peaks, which align with the S bonding form in the SO_3 structure of SBMA. In short, the characterization confirmed the introduction of zwitterionic structure onto PET surface *via* Schiff-base reaction.

3.3. Protein resistance and lubricating property of PEI-*g*-SBMA/TA–Fe^{3+}/PET surfaces

Non-specific protein adhesion on biomaterial surfaces is a critical factor in bacterial adhesion, biofilm formation, and inflammation. Compared with BSA adsorption of PET and TA–Fe^{3+}/PET surfaces, following the introduction of zwitterionic polymer, a significant reduction was easily observed (Fig. 5a). The BSA adsorption on PET surface was 54.39 mg cm^{-2} which may lead to the adhesion of bacteria and biological proteins. After deposition of TA–Fe^{3+} complex, PET surface did not significantly solve the issue of non-specific protein adhesion. Meanwhile, BSA adsorption of PEI-*g*-SBMA$_{12\%}$/TA–Fe^{3+}/PET

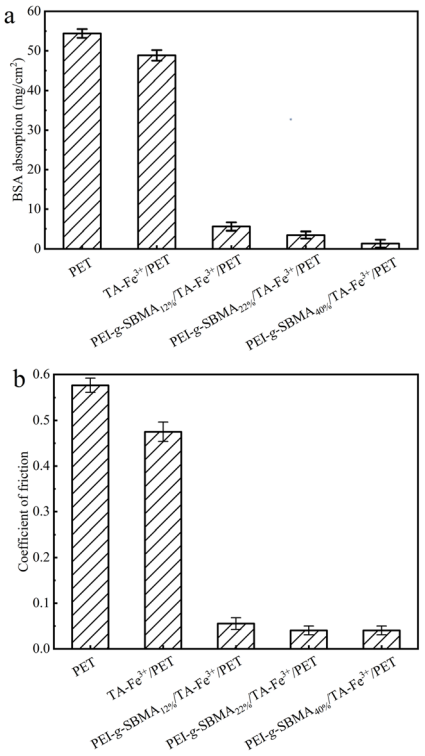

Fig. 5 BSA absorption of surfaces (a); coefficient of friction of surfaces (b).

reduced to 5.61 mg cm^{-2}. With the increasing grafting ratio of SBMA, the ion solvation effect became more pronounced. PEI-*g*-SBMA$_{40\%}$/TA–Fe^{3+}/PET showed a further reduction in BSA adsorption to 1.34 mg cm^{-2}. This phenomenon can be attributed to the zwitterionic polymer molecules, which possess both positive and negative charges on the same monomer unit. These charges interact with water molecules *via* electrostatic induction, forming stable, tightly aligned opposite charges. The uniform distribution of charges and the overall charge neutrality of these oppositely charged adhesion by blocking the electrostatic and hydrophobic interactions between proteins and the material surface. Furthermore, the steric hindrance effect of the zwitterionic polymer, combined with its hydrophilicity and mobility, results in a large exclusion volume.[42] When large molecules such as proteins come into contact with the polymer, the exclusion volume is compressed. This leads to an increase in the system's Gibbs free energy, causing the polymer chains to tend toward their original expanded state. This further assists in preventing the contact of pollutants.[43] The antifouling property are effectively achieved by introducing zwitterionic polymers on the surface. Similarly, due to the dense hydrated layer formed by the zwitterionic polymer surface, the friction coefficient of the surface also decreased. As shown in Fig. 5b, the friction coefficient of the PEI-*g*-SBMA$_{40\%}$/TA–Fe^{3+}/PET surface decreased to 0.04. This excellent lubricity can effectively prevent shear damage to tissues during catheter insertion and implantation, significantly reducing the potential for subsequent inflammation.

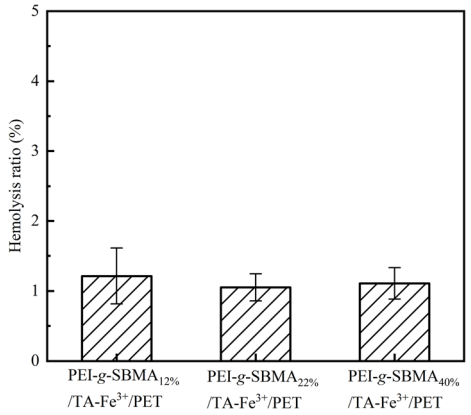

Fig. 6 Hemolysis ratio of PEI-*g*-SBMA$_x$/TA–Fe^{3+}/PET.

3.4. Hemocompatibilty of PEI-*g*-SBMA/TA–Fe^{3+}/PET

The hemolysis test was used to evaluate the hemocompatibilty of PEI-*g*-SBMA/TA–Fe^{3+}/PET. As shown in Fig. 6, the hemolysis ratio of all PEI-*g*-SBMA/TA–Fe^{3+}/PET samples were below 5%. According to the ISO10993-4, the hemolytic ratio must be lower than 5% for clinical application. Tannic acid (TA), a natural polyphenol, is widely employed in biomedical applications, including nanoparticle drug delivery systems for cancer treatment. On the other hand, SBMA is a promising material for applications in biosensing, temperature-sensitive materials, and other fields. Therefore, the coatings do not compromise the inherent biocompatibility of the material, and the modified medical materials demonstrate strong potential for clinical use.

4. Conclusions

In this paper, hydrophilic and antifouling surfaces were constructed inspired from tannic acid and zwitterionic polymer. Firstly, the stable TA–Fe^{3+} complex layers were deposited on the PET surfaces. Then the synthesized zwitterionic graft copolymer PEI-*g*-PSBMA was covalently linked to the TA–Fe^{3+} film *via* Schiff-base reaction, resulting in stable, biofouling functional surfaces. The TA–Fe^{3+} film provided excellent hydrophilic property while acting as a stable adhesion mediator between the zwitterionic polymers and the surfaces. The zwitterionic polymers suppressed the non-specific adsorption of proteins on the surfaces. Additionally, excellent hemocompatibility of suggested that the coatings were potential applications for biomedical fields. Thus, this strategy provides a commonly route for hydrophilic and antifouling modification of different materials surface.

Data availability

All data generated or analyzed during this study are include in this manuscript file.

Conflicts of interest

The authors declare no conflict of interest.

Acknowledgements

The authors thank the State Key Laboratory of Chemical Engineering of Zhejiang University for its support in providing characterization. The authors thank Dr Yangfan Lu (School of Materials Science and Engineering of Zhejiang University) for her help on XPS measurement and analysis.

References

1 J. W. Park, J. U. Hwang, J. H. Back, S. W. Jang, H. J. Kim, P. S. Kim, S. Shin and T. Kim, *Compos. B Eng.*, 2019, **178**, 107449.
2 Z. J. Yan, M. M. Yao, Z. M. Zhao, Q. Yang, R. Liu, B. J. Liu, X. Y. Wang, L. M. Chen, H. Zhang, Y. P. Wei, F. L. Yao and J. J. Li, *Adv. Healthcare Mater.*, 2024, **13**, 2400126.
3 M. H. Bai, B. S. Zhao, Z. Y. T. Liu, Z. L. Zheng, X. Wei, L. L. Li, K. Li, X. R. Song, J. Z. Xu and Z. M. Li, *Adv. Mater.*, 2022, **34**, 2108848.
4 B. S. Zhao, Y. P. Li, Q. N. Wang, Y. Ren, Z. L. Zheng, M. H. Bai, J. C. Lv, K. Li, J. Z. Xu, Z. M. Li and X. R. Song, *Chem. Eng. J.*, 2022, **427**, 130911.
5 J. Song, B. Winkeljann and O. Lieleg, *Adv. Mater. Interfaces*, 2020, **7**, 2000850.
6 S. S. Zhou, S. H. Qian, W. Wei, Z. F. Ni and J. H. Yu, *Langmuir*, 2021, **37**, 13493–13500.
7 G. P. Parada, Y. Yan, W. Riley, S. Lojovich, D. Tshikudi, Q. Ling, Y. F. Zhang, J. X. Wang, L. Lei, Y. Y. Yang, S. N. Nadkarni, C. Nabzdyk and X. H. Zhao, *Adv. Healthcare Mater.*, 2020, **9**, 2001116.
8 Y. Q. Zhang, J. Man, J. L. Wang, J. N. Liu, X. Z. Song, X. H. Yu, J. Y. Li, R. J. Li, Y. H. Qiu, J. F. Li and Y. G. Chen, *Int. J. Biol. Macromol.*, 2023, **254**, 127653.
9 J. R. Miao, X. Wu, Y. Fang, M. Z. Zeng, Z. M. Huang, M. Ouyang and R. Wang, *J. Mater. Chem. B*, 2023, **11**, 3373–3386.
10 H. L. Fan, J. H. Wang, Z. Tao, J. C. Huang, P. Rao, T. Kurokawa and J. P. Gong, *Nat. Commun.*, 2019, **10**, 5127.
11 Q. S. Li, C. Y. Wen, J. Yang, X. C. Zhou, Y. N. Zhu, J. Zheng, G. Cheng, J. Bai, T. Xu, J. Ji, S. Y. Jiang, L. Zhang and P. Zhang, *Chem. Rev.*, 2022, **122**, 17073–17154.
12 Q. Shao and S. Y. Jiang, *Adv. Mater.*, 2015, **27**, 15–26.
13 J. B. Schlenoff, *Langmuir*, 2014, **30**, 9625–9636.
14 P. Weber, M. Asadikorayem and M. Zenobi-Wong, *Adv. Healthcare Mater.*, 2024, **28**, 2401623.
15 L. Mi and S. Y. Jiang, *Angew. Chem. Int. Ed.*, 2014, **53**, 1746–1754.
16 T. H. Kim, J. H. Moon, S. Y. Han and K. C. Song, *Thin Solid Films*, 2024, **801**, 140422.
17 K. You, H. T. Meng, Z. Y. Du, W. T. Zhang, Q. Ma, Y. T. Huang, L. X. Cui, Y. F. Lei and Z. L. Yang, *Bioact. Mater.*, 2024, **37**, 493–504.
18 T. He, X. Y. Wang, Z. Y. Sun, W. J. Chen, M. Y. Cheng, Q. Chen, R. Z. Chen, Q. G. Li and Z. L. Cui, *J. Membr. Sci.*, 2024, **704**, 122891.
19 Y. Li, Y. P. Bai, X. Liu, Y. Q. Zhang, Y. P. Tang, F. Zhao, Q. H. Li, Z. G. Guo, Z. J. Feng, A. J. Dong, D. L. Kong,

W. W. Wang and P. S. Huang, *Compos. B Eng.*, 2023, **257**, 110670.
20 Y. F. Qian, J. Zhao, L. Liu, H. Hu, B. Wang and H. Y. Zhang, *Langmuir*, 2022, **38**, 3597–3606.
21 R. Zhou, P. F. Ren, H. C. Yang and Z. K. Xu, *J. Membr. Sci.*, 2014, **466**, 18–25.
22 L. Cheng, C. Liu, J. Wang, Y. Wang, W. H. Zha and X. S. Li, *ACS Appl. Polym. Mater.*, 2022, **4**, 3462–3472.
23 M. M. Yao, Z. J. Wei, J. J. Li, Z. C. Guo, Z. J. Yan, X. Sun, Q. Y. Yu, X. J. Wu, C. J. Yu, F. L. Yao, S. Q. Feng, H. Zhang and J. J. Li, *Nat. Commun.*, 2022, **13**, 5339.
24 X. W. Wang, J. Wang, Y. Yan, L. Yu, Y. X. Wang, K. F. Ren and J. Ji, *Nat. Commun.*, 2022, **13**, 5339.
25 B. Y. Chen, K. Lei, D. D. Zhu, C. C. Yang, C. Y. Sun, W. Xiao, Z. Zhen and X. L. Wang, *Adv. Mater. Interfaces*, 2021, **8**, 2100657.
26 R. N. Xu, Y. L. Zhang, S. H. Ma, Z. F. Ma, B. Yu, M. R. Cai and F. Zhou, *Adv. Mater.*, 2022, **34**, 2108889.
27 Y. Xie, C. Q. Tang, Z. H. Wang, Y. T. Xu, W. F. Zhao, S. D. Sun and C. S. Zhao, *J. Mater. Chem. B*, 2017, **5**, 7186–7193.
28 Y. X. Zhang, W. Jiang, L. L. Lei, Y. Wang, R. N. Xu, L. Qin and Q. B. Wei, *Langmuir*, 2022, **38**, 7157–7167.
29 H. Ejima, J. J. Richardson, K. Liang, J. P. Best, M. P. van Koeverden, G. K. Such, J. W. Cui and F. Caruso, *Science*, 2013, **341**, 154–157.
30 S. Q. Chen, Y. Xie, T. J. Xiao, W. F. Zhao, J. S. Li and C. S. Zhao, *Chem. Eng. J.*, 2018, **337**, 122–132.
31 Z. Y. Song, X. Kong, Y. Xue, Z. Y. Yin, C. C. Sun, J. J. Yuan, B. K. Zhu and L. P. Zhu, *Colloids Surf., A*, 2017, **522**, 585–592.
32 Y. R. Xiao, D. X. Guo, T. Li, Q. F. Zhou, L. G. Shen, R. J. Li, Y. C. Xu and H. J. Lin, *Appl. Surf. Sci.*, 2020, **515**, 146063.
33 H. J. Kim, D. G. Kim, H. S. Yoon, Y. S. Choi, J. Y. Yoon and J. C. Lee, *Adv. Mater. Interfaces*, 2015, **2**, 1500298.
34 Y. Xie, S. Q. Chen, X. Zhang, Z. Q. Shi, Z. W. Wei, J. X. Bao, W. F. Zhao and C. S. Zhao, *Ind. Eng. Chem. Res.*, 2019, **58**, 11689–11697.
35 A. Venault, H. S. Yang, Y. C. Chiang, B. S. Lee, R. C. Ruaan and Y. Chang, *ACS Appl. Mater. Interfaces*, 2014, **6**, 3201–3210.
36 T. Ma, Y. Su, Y. Li, R. Zhang, Y. Liu, M. He, Y. Li, N. Dong, H. Wu and Z. Jiang, *J. Membr. Sci.*, 2016, **503**, 101–109.
37 M. Krogsgaard, A. Andersen and H. Birkedal, *Chem. Commun.*, 2014, **50**, 13278.
38 J. W. Yang, R. B. Bai, B. H. Chen and Z. G. Suo, *Adv. Funct, Mater.*, 2020, **30**, 1901693.
39 K. Dey, S. R. Chowdhury, E. Dykstra, A. Koronatov, H. P. Lu, R. Shinar, J. Shinar and P. Anzenbacher, *J. Mater. Chem. C*, 2020, **8**, 11988–11996.
40 K. Dey, S. R. Chowdhury, E. Dykstra, H. P. Lu, R. Shinar, J. Shinar and P. Anzenbacher, *ACS Appl. Electron. Mater.*, 2021, **3**, 3365–3371.
41 N. Marques, S. Jana, M. J. Mends, H. Aguas, R. Martins and S. Panigrahi, *RSC Adv.*, 2024, **14**, 12397–12406.
42 Y. N. Chou and M. Z. Ou, *ACS Appl. Mater. Interfaces*, 2023, **5**, 5411–5428.
43 M. R. He, K. Gao, L. J. Zhou, Z. W. Jiao, M. Y. Wu, J. L. Gao, X. D. You, Z. Y. Cai, Y. L. Su and Z. Y. Jiang, *Acta Biomater.*, 2016, **40**, 142–152.